2018

Global tectonic reconstructions with continuously deforming and evolving rigid plates

Michael Gurnis
California Institute of Technology

Ting Yang
California Institute of Technology

John Cannon
University of Sydney

Mark Turner
California Institute of Technology

Simon E. Williams
University of Sydney

See next page for additional authors

Publication Details

Gurnis, M., Yang, T., Cannon, J., Turner, M., Williams, S., Flament, N. & Muller, R. (2018). Global tectonic reconstructions with continuously deforming and evolving rigid plates. Computers and Geosciences, 116 32-41.

Global tectonic reconstructions with continuously deforming and evolving rigid plates

Abstract
Traditional plate reconstruction methodologies do not allow for plate deformation to be considered. Here we present software to construct and visualize global tectonic reconstructions with deforming plates within the context of rigid plates. Both deforming and rigid plates are defined by continuously evolving polygons. The deforming regions are tessellated with triangular meshes such that either strain rate or cumulative strain can be followed. The finite strain history, crustal thickness and stretching factor of points within the deformation zones are tracked as Lagrangian points. Integrating these tools within the interactive platform GPlates enables specialized users to build and refine deforming plate models and integrate them with other models in time and space. We demonstrate the integrated platform with regional reconstructions of Cenozoic western North America, the Mesozoic South American Atlantic margin, and Cenozoic southeast Asia, embedded within global reconstructions, using different data and reconstruction strategies.

Disciplines
Medicine and Health Sciences | Social and Behavioral Sciences

Publication Details
Gurnis, M., Yang, T., Cannon, J., Turner, M., Williams, S., Flament, N. & Muller, R. (2018). Global tectonic reconstructions with continuously deforming and evolving rigid plates. Computers and Geosciences, 116 32-41.

Authors
Michael Gurnis, Ting Yang, John Cannon, Mark Turner, Simon E. Williams, Nicolas Flament, and R. Dietmar Muller

Global Tectonic Reconstructions with Continuously Evolving Deforming and Rigid Plates

Michael Gurnis[a,1], Ting Yang[a,2], John Cannon[b], Mark Turner[a], Simon Williams[b], Nicolas Flament[b,3], and R. Dietmar Müller[b]

a. Seismological Laboratory, California Institute of Technology, Pasadena, CA 91125, USA

b. EarthByte Group, School of Geosciences, The University of Sydney, Sydney, NSW 2006, Australia

1. *Corresponding author: gurnis@gps.caltech.edu*
2. *Now at: School of Earth Sciences, University of Melbourne, Melbourne, Vic 3010, Australia*
3. *Now at: School of Earth and Environmental Sciences, University of Wollongong, Northfields Avenue, Wollongong NSW 2522, Australia.*

Abstract. Traditional plate reconstruction methodologies do not allow for plate deformation to be considered. Here we present software to construct and visualize global tectonic reconstructions with deforming plates within the context of rigid plates. Both deforming and rigid plates are defined by continuously evolving polygons. The deforming regions are tessellated with triangular meshes such that either strain rate or cumulative strain can be followed. The finite strain history, crustal thickness and stretching factor of points within the deformation zones are tracked as Lagrangian points. Integrating these tools within the interactive platform *GPlates* enables specialized users to build and refine deforming plate models and integrate them with other models in time and space. We demonstrate the integrated platform with regional reconstructions of Cenozoic western North America, the Mesozoic South American Atlantic margin, and Cenozoic southeast Asia, embedded within global reconstructions, using different data and reconstruction strategies.

Key words: Plate tectonics, continental drift, geophysics, geodynamics, paleogeography, lithosphere.

1. Introduction

Plate tectonics is the fundamental representation of motion and deformation of Earth's surface over at least the last several geological time periods (Wessel and Müller, 2015) and we rely on software to visualize, manipulate and analyze a wide variety of data to build plate models constrained by observations. A diverse range of fundamental and applied research questions in geology, geophysics, geochemistry, paleontology, and hydrocarbon and mineral exploration are routinely addressed with such software. Increasingly, such software is also being used as an interface between plate reconstructions and global and regional computational models of geodynamic (e.g. Bower et al., 2015) and climate change (e.g., Lunt et al., 2017) processes, while being an unusually effective educational tool for Earth history. Animations developed from such plate reconstructions have become a way to engage non-specialists on the significant achievements toward our understanding of Earth history, and interactive animations are available on the GPlates Portal (Müller et al., 2016b). It is essential that such plate tectonic software be continuously enhanced as scientific questions advance.

Surface tectonic evolution can mostly be described using the rules of plate motion as reflected in software aimed at working with plate tectonic reconstructions on a global scale (Torsvik and Smethurst, 1999; Lawver, 2001; Boyden et al., 2011; Williams et al., 2012). Within a substantial fraction of the surface, however, the assumption of plate rigidity is not satisfied and deformation is diffuse. It is estimated that about 15% of Earth's surface area today is deforming in wide deformation zones (Gordon and Stein, 1992) in a variety of settings via crustal stretching, compression or a combination of the two often with block rotation. Regional and local models of these zones of deformation have been created (e.g., Arriagada *et al*., 2008; Kneller *et al*., 2012; Replumaz and Tapponnier, 2003; Xu *et al*., 2014). Often plate tectonic rates are used to constrain these deformations as either displacement rates on the edges of the zones of deformation or as integral constraints over the extent of these zones. Regional deformation models have been created with two kinds of representations: as a set of rotating and

displacing blocks (often rigid blocks) or as a continuous deformation field, akin to that of a deforming fluid (Thatcher, 2009). As one of the largest zones of non-plate tectonic deformations, a variety of such models have been developed to understand the deformation of the Himalayan region (e.g., Replumaz and Tapponnier, 2003; Holt *et al.*, 2000). For the present day, several attempts have been made to characterize plate deformations in a global sense, especially since the wide use of GPS measurements (see review by Thatcher, 2009). Most notable is the global strain rate model (GSRM-1 and its update 2.1) using GPS, geological and seismic observations in conjunction with a global model of rigid plate motions (Kreemer, *et al*. 2003, 2014). In this model, a least squares analysis is performed over rigid and deforming regions of Earth's surface to obtain a continuous field of deformation. The GSRM approach is powerful and is used to address questions ranging from how contemporary rates of deformation are related to seismic hazards to the causes of plate deformation (Kreemer *et al*., 2003, 2014).

Regional models of plate deformation have been fundamental in characterizing the nature of long-term deformation and the mechanical condition of the lithosphere, but there is a distinct need to incorporate these models into time-dependent global models. Here we describe our attempt to do that using the plate tectonic modeling program *GPlates* (Boyden *et al*., 2011) in which individual regions of plate deformation are embedded into the global model. This method has recently been used in several studies in which the plate models are used in conjunction with four-dimensional computations of mantle, lithosphere and crustal deformation (Flament *et al*., 2014; Yang *et al*., 2016). The method builds directly on the *GPlates* concept of a continuously evolving plate polygon in which the edges of each plate is continuously followed and at each moment the polygonal outline closed (Gurnis *et al*., 2012). Rigid plate polygons are replaced with a continuously deforming field, although internally deforming region maybe represented by any number of deforming and rigid elements.

2. Deforming Regions

Consider a single deforming region bounded by rigid plates. Each one of these boundaries can be represented by a set of line elements in which lines move with a single pole of rotation or the line is made up of points each with a different rotation pole. Together, all of these lines make a closed polygon. If a rigid plate exists within the entire domain bound by the polygon, then this is a continuously closed plate as described within *GPlates* (Gurnis *et al*., 2012). But, imagine that within this polygon, the region is undergoing deformation, either between a set of smaller internal rigid blocks undergoing differential motion, continuous deformation or some combination of the two. For illustration, this is made explicit in a schematic example (Fig. 1A) in which we have a deforming region D_1 with a left boundary defined as a subducting plate, P_3, dipping to the right, characterized by a set of points, some of which rotate with $\omega_1^M \ldots \omega_n^M$. In the example, superscripts refer to the class of the moving entity (*M* for margin and *D* for deformation zone) and subscripts are explicit entities since Earth's surface is made up of many plates and deforming regions at any moment of time. The rest of the boundary is composed of a series of smaller lines, perhaps faults each with their own motion. Within the deformation zone D_1 there is a number of geological entities, including a rigid block (RB) that moves with respect to some point on the boundary with a local velocity, u_4. Within the deforming region the space between any rigid blocks and the boundaries of D_1 are occupied by a set of points and lines each of which moves with their own velocity. Each of the velocities that constitute the boundary and interior are defined by a rotation about an Euler pole for some period of time; for clarity and as a means to construct deforming regions with observations, those rotations are with respect to an adjacent rigid plate. In the example, the plate to the right, P_1, is rigid and we assume that the motions within D_1 are referenced with respect to P_1. At any moment of time the lines and points that define the boundary must be closed as a polygon (Fig. 1B). The exact point of intersection between line elements is continuously determined (red dots, Fig. 1B) and *GPlates* fills gaps between data lines with automatically generated ones (short red lines). The boundary between a

deforming zone and rigid plate is often imperfectly defined (geologically), and there may be a gradation between deforming and ideal rigidity, as the boundary between D_1 and P_1. This is represented by a small set of constraints within the diffuse boundaries which are represented as small lines that do not form a continuous, connected line between D_1 and P_1 (black lines, Fig. 1). Consequently, the closing polygon algorithm will connect adjacent line segments (red lines, Fig. 1). Now, the entire remaining area between all of the edge points (those within boundary lines and individual points) and any number of non-overlapping rigid blocks is represented by a space filling triangulation (green triangles, Fig. 1B). The rotations and hence local velocity are now defined entirely through linear interpolation within each triangle. In *GPlates*, the representation of a deforming region is called a *Topological Network*. The algorithms and methods described here have been implemented in the open source *GPlates Version 2.1* and are available for download at the links on http://www.gplates.org.

3. Plate rotations, strain rate and deformation history

A plate tectonic reconstruction program like *GPlates* needs to use several computational strategies to efficiently and continuously rotate and visualize plate tectonic data. Most important is that *GPlates* uses a rotation tree and rotates each point and line data in real time from the present to its past position (Boyden et al., 2011). All underlying plate tectonic data are stored using their present day coordinates. This allows users interacting with the visualization on screen to seamlessly animate plate tectonic data either going forward or backward in time. Once local motions of the points, lines and polygonal outlines of rigid blocks (Fig. 1A) are converted to rotations about an Euler pole (Fig. 1B) and then placed within the rotation tree, all of the information within the deforming zones can be manipulated and visualized as any other plate tectonic data with *GPlates*. Moreover, the gradient of the velocity field (strain rate, Appendix A) can also be instantly computed and visualized on screen.

An important use of the software is the iterative development of the plate reconstruction itself by specialists with intimate knowledge of the global, regional or local geology. Regional geological reconstructions of deformation are generally built up with a set of inferred, local displacements each of which tends to have considerable uncertainty, which we view as geological noise, processes not related to the regional deformation. Strain rates tend to be a derived quantity from a reconstruction of a deformation zone often determined from strain markers and other integrated outcomes of deformation (such as rock offsets, rock foliation, crustal thickness, tectonic subsidence, paleomagnetic rotations, etc). Consequently, strain rates between adjacent spot observations tend to show considerable variations in time and space. Less noisy representations of deformation are the displacement rates ("plate velocity" of the local point), smoothed strain rate fields and quantities integrated in time. In addition, if we integrate finite strain points through a smoothed strain rate field we then have a strain representation with smoothing in time and space.

We have built tools that allows users to work with the integrated outcomes of deformation (Appendix B). This means that we needed to build upon the standard device of continuously rotating data from the present to the past. Any observation point in which we have some estimate of finite strain is represented by its present day coordinate, like any other *GPlates* data, but within the interior of a deforming topological network. This means that in general, the paleo-position of an observation point must be determined by interpolating rotations from nearby points with known rotations. So, the first step is to sequentially integrate a point backward in time through the interpolation of rotations (Step 1 in Fig. 2), which makes possible the determination of its initial position (or initial condition, IC) in the past. For the IC, we assume the point has no strain. Then, the position of this point is integrated forward in time and the point accumulates finite strain (represented as a tensor) as it moves through the deformation field while undergoing deformation (Step 2, Fig. 2). This is akin to following a Lagrangian particle, for example in a deforming solid or fluid (Malvern, 1969). In *GPlates*, these data (*e.g.* history, position and

strain) are computed after the time of appearance of a strain marker that has been assigned to a deforming topological network and these data are retained for subsequent retrieval during a forward or backward onscreen animation. The strain history can now be visualized on screen. The only downside of this approach is that as a geologist interactively manipulates the underlying data within a deforming topological network, like moving a point around or changing the rotation pole, the history must be recomputed. This involves a slight pause in the operation of *GPlates* as the strain history is recomputed and stored, but that pause is only several seconds (or less) for the models shown here on current generation laptops and workstations and is not deemed to be an impediment for efficient animations or the development of reconstructions.

4. Software elements for Deforming Topological Networks

The modules for Deforming Topological Networks within *GPlates* were developed as an extension of continuously closing plates (Gurnis *et al*., 2012) and used a combination of new code and software libraries. As described earlier, resolving a topological boundary means traversing its list of boundary sections at a particular geological time and intersecting adjacent sections to form a resolved boundary polygon for that geological time (Gurnis *et al*., 2012). And since the boundary sections typically move independently over time, the shape of the resolved polygon also changes over time. The boundary of a deforming topological network is also resolved using this same technique.

Building topological boundaries is now easier with the introduction of the *topological line,* which is similar to a topological boundary except it is not closed to form a polygon (it is essentially a continuously closing *line*). In this way a topological line can gather independently rotating boundary points that represent a non-rigid section of a network boundary (see boundary between P_3 and D_1 in Fig. 1). This means a single topological line can, in turn, be inserted as part of a topological boundary rather than having to insert each point individually, thus reducing the work required to build a deforming network

boundary. Interior points, lines and polygons do not need to intersect since they are only used to constrain the continuous deformation field inside the network. Additionally, interior polygons are classified as rigid blocks (RB in Fig. 1) and hence automatically excluded from the continuous deformation field.

To model the continuous deformation field, a Delaunay triangulation at a particular geological time is created using all points from a network's resolved boundary polygon and all its interior geometries (including rigid blocks, Fig. 1B). We use the 'Delaunay_triangulation_2' class in the Computational Geometry Algorithms Library (CGAL) (Fabri and Pion, 2009; The CGAL Project, 2017) to create Delaunay triangulations after projecting 3D points (on the sphere) to 2D coordinates using the Lambert Azimuthal Equal Area projection (with a projection center matching the centroid of the network boundary). Since a Delaunay triangulation is actually a convex hull (2D) of these boundary and interior points, we only consider those Delaunay faces that contribute to the continuous deformation region between the network boundary and any interior rigid blocks (green triangles in Fig. 1B).

An arbitrary point (for example, an inserted point not associated with the original data) inside the deforming region can be deformed over an incremental time interval (typically one million years) by (i) calculating the Barycentric coordinates of the Delaunay face containing that point, then (ii) rotating the three vertices of the face over a time increment (according to their velocities) and finally (iii) using Barycentric interpolation of the new face vertex positions to determine the deformed point position. This incremental method of deformation can then be accumulated through time to build a history of deformed positions that are stored in a lookup table. This enables arbitrary geometries to be placed within a topological network and deformed over geological time. Another type of point query is calculating the velocity at an arbitrary point inside the deforming region. In this case, a natural neighbor interpolation of the velocities of the associated Delaunay vertices is performed.

The velocities of the three vertices of a Delaunay face determine its strain rate. This means the strain rate is constant across each face and may change abruptly from face to face, so the user has the option to

smooth the strain rates. When smoothing is chosen, smoothed strain rates are first calculated at Delaunay vertices using a face-area average of triangles incident to each vertex. Then, either Barycentric or Natural Neighbor interpolation is performed between Delaunay vertices with Natural Neighbor interpolation providing a wider coverage of nearby vertices and thus smoother strain rates.

5. Examples of Regional Deforming Topological Networks in *GPlates*

Regional deforming topological networks can be developed with different data sets and workflows and placed within the context of global plate motion in which Earth's surface is mostly covered with rigid plates at any moment of time. The first example, from Cenozoic western North America, shows how a previously generated and published detailed geological reconstruction can be imported and placed within a global model. The second example from Cenozoic southeast Asia, shows how we can develop a model from scratch using both plate tectonic motions, basin subsidence, and paleo-magnetic rotations. Finally, we show how we can use present day geophysical observations of continent-ocean boundaries (COB) and combine them with plate tectonic rotations to reconstruct the rifting between South America and Africa. These methods of generating and importing regional deforming models are not necessarily the only pathways, but are the ones we have explored so far.

5.1 Western North America. We use an existing regional reconstruction in which the deformation details have been published and made available digitally (McQuarrie and Wernicke, 2005), illustrating the value of building directly on the work of those with detailed local knowledge of a region. McQuarrie and Wernicke (2005) augmented local strain markers from earlier studies (Wernicke et al., 1988; Snow and Wernicke, 1998) to build a set of deformation points across three east west transects of the Basin and Range province of south western United States from 36 Ma to the present. The Basin and Range province has undergone extension during the Cenozoic with extensive exposure of metamorphic core complexes.

Individual strains were pieced together to create displacements as a function of age with respect to stable North America. Adjacent to the Basin and Range province, the displacements were augmented with rigid block displacement and rotation of the Sierra Nevada Block and the Colorado Plateau as well as with the San Andreas fault-Gulf of California shear system and the California Borderlands. McQuarrie and Wernicke (2005) provided the location of the displacement points, outlines of rigid blocks as GIS shape files, and displacement velocities in kilometers east and north of stable North America. All local and regional reconstructions are limited in extent and expose uncertainties and incompatibilities at their edges, a point highlighted by McQuarrie and Wernicke (2005). In order to attempt to merge their reconstruction with the global model, we used their boundary between stable North America and the region of Cenozoic deformation as one of the boundaries of the topological network and added in the rotation of several additional blocks, in particular the Cascade arc and the Klamath in which we used the rotations in Atwater and Stock (1998); we made no attempt to resolve the details between the Cascade Arc and stable North America, a domain for future refinements of this generalized reconstruction.

Since the underlying displacement points of McQuarrie and Wernicke (2005) were given in velocity east and north of the eastern edge of the deforming topological network, these displacement rates were transformed to Euler rotations with respect to stable North America (Fig. 3A). With the interior displacement points and points along the edges of the rigid blocks the deformation network (Fig. 3B) can be rotated backward in time to 36 Ma (Fig. 3C). For illustration, we then placed a finite set of strain markers within the deforming zone and their reconstruction paths recovered and then forward integrated to obtain their finite strains (Fig. 3D).

The final display (Fig. 3D) illustrates several features of reconstructions with inherently noisy data. Within the broad region of Basin and Range extension, several high frequency patches of compression emerge between the Sierra Nevada and the Colorado Plateau, even with spatial smoothing, presumably related to the finite and noisy nature of the underlying constraints. We view these edge effects, which

currently may be incompatible with geological constraints, an advantage of the method, as they will become obvious rapidly to the specialist working with detailed knowledge of the region and allow him/her to rapidly explore reconstruction alternatives and improvements rapidly. The user can qualitatively judge which areas of deformation (Fig. 3B) are better constrained through the density of the vector constraints (Fig. 3A). In addition, the finite strains show either progressive compression or tension with no incompressibility constraint imposed and reflecting the overall extension in the region with zones of compression along the San Andreas Fault. A key aspect of the integration of these algorithms is the ability to integrate into the global perspective, as shown for the western North America deforming topographical network within the context of the surrounding plates at 26 Ma, for example (Figure 4).

5.2 Southeast Asia. Sundaland, the continental core of southeast Asia, is deforming only slowly at the present, as evidenced by low seismicity and strain rates from GPS observations (Simons et al., 2007). However, Sundaland experienced complex and intense deformation during the Cenozoic. Widespread extension developed within Sundaland since the late Eocene forming numerous rift basins (Hall and Morley, 2004; Doust and Sumner, 2007). Since the early Miocene, the region suffered widespread compression with many of these basins undergoing inversion, concurrent with the submersion of the entire Sunda shelf (Hall and Morley, 2004; Doust and Sumner, 2007), possibly in response to mantle processes (Yang et al., 2016).

The Sundaland deforming topological network boundaries coincide with southeast Asian continental edges at present (Fig. 5A). We used two sets of features to reconstruct the internal deformation history of Sundaland since 40 Ma: sedimentary basin boundaries and rigid blocks describing regions that experienced little deformation during the Cenozoic. The rigid block motion history based on paleomagnetic data are used to infer the motion of the Indo-China rigid block relative to South China during the Cenozoic (Lee and Lawver, 1994). Reconstructing the motion of Borneo relative to Sumatra

is primarily based on paleomagnetic data that suggests ~50º counterclockwise rotation of Borneo since 25 Ma (Fuller et al., 1999) and interpretation of curved structural lineaments in Java Sea in the gravity field as a result of oroclinal bending (see Zahirovic et al., 2014) which synthesized previous regional reconstructions (Lee and Lawver, 1994; Hall, 2002; Metcalfe, 2011) and embedded the regional rigid plate reconstruction model to the global reconstruction (Seton et al., 2012). There is a known incompatibility between the paleomagnetic and geological data (Morley, 2002) and our reconstruction incorporates the full 50º counterclockwise with commensurate large values in deformation around Borneo (Fig. 5D). The rifting history (strain rate, stretching factor) of Cenozoic basins (Fig. 5A) throughout SE Asia can be inferred from tectonic subsidence curves. Fixing one boundary of the rifting basin to the adjacent rigid block, the moving history of the other approximately sub-parallel basin boundaries is inferred based on the inferred strain rate and stretching factor (Yang et al., 2016). Although only a limited number of features (rigid block, basin boundaries) have the prescribed motion history based on geological datasets, *GPlates* automatically describes the whole deforming topological network with Delaunay triangulations and calculates the motion and deformation history of any point within the deforming network with linear interpolation of the displacement field (Figs 5B, C). The dilatational strain rate is low at present (Fig. 5B), however during the Oligocene basins across Sundaland were undergoing significant extension while the Malay Peninsula was under compression (Fig. 5C) (Cottam et al., 2013). A group of strain markers are generated within the deforming network to record the evolution of accumulated quantities (*e.g.* crustal thickness, β factor, finite strain) inside the deforming network. The stretching (β) factor, defined as the ratio of the width of a crustal block after the deformation to it's initial value, is computed for these strain markers at 0 Ma (Fig. 5D). β factor is large in sedimentary basins but low in regions of predicted strong compression. Although the present internal strain rate is small, the accumulated finite strain at strain markers records the magnitude and direction of intensive extensional (red) or compressional (blue) deformation history in Sundaland (Fig. 5D). The

strong compression between Malay Peninsula and Borneo is inconsistent with regional geological investigations (Hall and Morley, 2004), highlighting incompatibilities in the model of southeast Asia deformation. Considering the small amount of compression in this region, Hall and Moreley (2004) allowed only ~25º counterclockwise rotation of Borneo, although paleo-magnetic records suggest ~50º counterclockwise rotation of Borneo since 25 Ma (Fuller et al., 1999).

5.3 South Atlantic. To reconstruct the rifting and breakup between major continents, it is crucial to account for extensional deformation with wavelengths that are typically several hundred kilometers (e.g. Dunbar and Sawyer, 1987; Williams et al, 2011). This deformation results in regions of thinned crust within passive continental margins, bounded on the landward side by thick, undeformed continent, and on the oceanward side by a transition to oceanic crust formed by seafloor spreading. In the case of the opening the South Atlantic Ocean, a further complication arises from internal deformation recorded within Africa and South America, contemporaneous with South Atlantic opening of sufficient magnitude to require that it must also be accounted for within regional reconstructions (*e.g.* Unternehr et al., 1988). Here, we illustrate a model for the rifting associated with South Atlantic breakup based on the kinematic reconstruction of Heine et al. (2013). The resulting reconstruction depends only on the rigid plate reconstruction kinematics, geometries defining the boundaries of extended crust in the rifted margins, and the assumption of pure shear extension within the deformed region. Line geometries defining the extent of deformation along conjugate passive margins, and within Africa and South America, are based on the definitions provided by Heine et al. (2013) and detailed in Flament et al. (2014). The deforming regions on each margin are bounded on the landward side by the interpreted limit of syn-rift deformation, and on the oceanward side by the limit of extended continental crust. By necessity we define the transition from continental (deformed) to oceanic (undeformed) crust as a discrete boundary, though these transitions are likely to be more complex in nature (*e.g.* Péron-Pinvidic and Manatschal, 2009). Continent

ocean boundaries (COBs) are expected to show large overlaps in simplified pre-rift reconstructions when syn-rift extension is not explicitly accounted for, and the challenge is to unravel the deformation such that two separate deformation networks, one spanning each of the conjugate margins, fit together in our reconstructions without gaps or overlaps. To achieve this we adopt a procedure to account for the implied deformation, similar to those described by Srivastava and Verhoef (1992) and Kneller et al (2012), and outlined in the following paragraph.

The rift kinematics for all elements of the deformation model are derived from the regional rift kinematics defined by Heine et al (2013). Deformation begins everywhere within the South Atlantic at 145 Ma as South America and Africa begin to diverge. Within each section of the margin, the overall period of deformation is defined by this rift onset and the time of breakup (which is controlled by the time at which the conjugate COBs no longer overlap with the conjugate). The timing of breakup is diachronous from south to north, and to describe this 'unzipping' in GPlates, we define a series of points along each COB which define the oceanward boundaries of the deforming network for each margin, and for which we compute individual finite rotations. If we consider a single point on one of these COBs, we can determine, from the regional kinematics and the geometries, at what reconstruction time this point will intersect with the COB on the conjugate margin. This time can be considered as a 'breakup' time, marking the end of deformation at this location along the margin. For example in Fig. 6A, B, breakup is achieved in the south of the illustrated region (such that the strain rate is zero here, labelled P in Fig. 6C) and a small ocean basin has begun to open, while deformation continues to the north (labelled DC in Fig. 6C). After the breakup time, the points can be considered as part of the passive (non-deforming) margin of their parent continent, and move with the same rigid rotation. Between the rift onset time and the breakup time deformation is implied between the conjugate rigid continents (Fig. 6C), and we assume that the direction of extension (and therefore the displacement trajectory of each COB point) at all times is defined by the stage pole defining the relative motion between these continental blocks at that time.

As in Srivastava and Verhoef (1992), the example shown here takes the simplest approach of assigning deformation linearly across the region that is considered to be deforming at any instant. A drawback of this approach is that the deforming regions representing breakup are pre-computed outside *GPlates* using separate workflows - this means that if the regional model defining the motion of the major plates (South America, Southern Africa, etc.) is modified then the kinematics of the points defining the deforming regions would need to be recomputed (as they would not be automatically updated by *GPlates*). This deforming topological network was used in global models of mantle flow and lithosphere deformation to compute the evolution of topography along the margins of the South Atlantic Ocean (Fig. 6D; Flament et al., 2014).

6. Discussion and Conclusions

Exploiting the methods in *GPlates*, in which the entire surface of the earth is covered by evolving dynamically closing plate polygons, we extend the approach from enclosing rigid plates to the case where some polygons are represented with deforming regions. The approach provides a framework to build and extend regionally deforming plate models, widely used for regional studies, into an interactive, global context. An important outcome of *GPlates* has been the wide availability of open source reconstruction tools and a format for the delivery of global reconstructions, allowing investigators to take published reconstructions and easily migrate them to their own work. Consequently, with the release of the deforming topological network features described here, *GPlates* 2.1 now allows that same flexibility to be available for deforming plate models integrated with global rigid ones. The approach opens the door to the first long time-scale global deforming plate models. Regional deforming models are best developed by those with intimate knowledge of the regional geology since much qualitative information is integrated with quantitative constraints and so the tools provided here will give much greater functionality to the development of such models.

Having embeded regional deformation models in global models is significant, as regional models can be made self-consistent with the motions of large plates (for example, for a deforming model in the Tethys, or Caribbean), with the plates around the deforming region set to the tectonic boundary conditions from the global model. Separating the internal points defining the deformation (especially if they are with respect to an adjacent rigid entity), allows for a greater ease in reconciling regional and global models. Similar to regional models, global models are continuously being updated (see review by Müller et al., 2016) and regional deformation models embedded within global models need to be continuously updated to ensure their consistency. Having regional data and global data in the same format will allow a much greater turnaround of such models and much greater model availability to other researchers. Reconstructions often need to be developed within the context of other data sets, such as mantle tomographic images or a region's relative movement with respect to mantle hotspots. Such constraints require a global frame of reference that the global reconstruction provides.

By the same token, regional reconstructions should find a much more seamless transition to those requiring a much larger perspective and the integration of regional models into global ones (e.g. Figure 4). Plate reconstructions are playing a much greater role in the steering and the validation of geodynamic models of the solid earth (Gurnis et al., 1998; Bunge et al., 2002; Moucha, et al., 2008) and general circulation models (GCMs) of the climate system (Godderis et al., 2014; Lunt, et a., 2017). Regions of deforming plates give rise to some of the largest changes in topography and have a disproportionate influence on changing atmospheric circulation patterns or providing the sinks for sediment deposition. Consequently, the accurate incorporation of regional deformation into models of the global earth system is essential. The new features introduced here will aid in such studies.

Acknowledgements. We would like to thank Nadine McQuarrie and Sascha Brune for helpful reviews which improved the manuscript. MG, TY and MT supported by the National Science Foundation under

EAR-1358646 and EAR-1645775 and by Statoil ASA. RDM and SW are supported by Australian Research Council grant IH130200012. NF was supported by Statoil ASA and by Australian Research Council grant DE160101020.

Appendix A. Instantaneous Deformation

Here we depict the instantaneous strain rate computations under spherical coordinates that is applied in the Deforming Topological Networks of *GPlates*. Following the strategy of finite element analysis with linear shape functions (e.g. Hughes, 2012), Delaunay triangulation is used to mesh a deforming network into a series of constant strain rate spherical triangle elements (Section 4). The velocity of each triangle vertex is calculated based on their stage rotations. The velocity and strain rate at any point inside the triangle can be uniquely determined from the velocity at these three vertexes. Divergence or convergence of the horizontal velocity field at a point on the spherical surface thin or thicken the lithosphere in the vertical direction (similar to plane stress, which is usually used for thin plates).

By definition, the three components of the strain rates (normal in the latitudinal and longitudinal directions, shear), dilatational strain rate and the second invariant of the strain rate of any point in spherical coordinates are expressed as

$$\dot{\varepsilon}_{\theta\theta} = \frac{\partial u_\theta}{R\partial\theta}\ \dot{\varepsilon}_{\theta\theta} = \frac{\partial u_\theta}{R\partial\theta} \tag{A1}$$

$$\dot{\varepsilon}_{\phi\phi} = \frac{1}{R\sin\theta}[u_\theta \cos\theta + \frac{\partial u_\phi}{\partial \phi}] \dot{\varepsilon}_{\phi\phi} = \frac{1}{R\sin\theta}[u_\theta \cos\theta + \frac{\partial u_\phi}{\partial \phi}] \tag{A2}$$

$$\dot{\varepsilon}_{\theta\phi} = \frac{1}{2R}[\frac{1}{\sin\theta}\frac{\partial u_\theta}{\partial \phi} + \frac{\partial u_\phi}{\partial \theta} - u_\phi \cot\theta] \dot{\varepsilon}_{\theta\phi} = \frac{1}{2R}[\frac{1}{\sin\theta}\frac{\partial u_\theta}{\partial \phi} + \frac{\partial u_\phi}{\partial \theta} - u_\phi \cot\theta] \tag{A3}$$

$$\begin{aligned} \dot{\varepsilon}_D &= \mathrm{div}(\vec{u}) = \frac{1}{R\sin\theta}[u_\theta \cos\theta + \sin\theta \frac{\partial u_\theta}{\partial \theta} + \frac{\partial u_\phi}{\partial \phi}] \\ \dot{\varepsilon}_D &= \mathrm{div}(\vec{u}) = \frac{1}{R\sin\theta}[u_\theta \cos\theta + \sin\theta \frac{\partial u_\theta}{\partial \theta} + \frac{\partial u_\phi}{\partial \phi}] \end{aligned} \tag{A4}$$

$$\dot{\varepsilon}_{II} = \sqrt{\dot{\varepsilon}_{\theta\theta}^2 + \dot{\varepsilon}_{\phi\phi}^2 + 2\dot{\varepsilon}_{\theta\phi}^2} \tag{A5}$$

Where θ, ϕ ϕ, u_θ, and u_ϕ u_ϕ represent colatitude, longitude, velocity in colatitude, and longitude directions, respectively. R is the average radius of the Earth.

Considering one point in a spherical triangular element, and, assuming that it has a corresponding projection to a Cartesian coordinate and the coordinate and velocity of this point under the spherical coordinate can be expressed as linear functions of its corresponding Cartesian coordinates, then the coefficients of the linear functions are determined by the values of the three vertexes:

$$\begin{cases} \phi = (\phi_2 - \phi_1)x + (\phi_3 - \phi_1)y + \phi_1 \\ \theta = (\theta_2 - \theta_1)x + (\theta_3 - \theta_1)y + \theta_1 \\ u_\phi = (u_{\phi 2} - u_{\phi 1})x + (u_{\phi 3} - u_{\phi 1})y + u_{\phi 1} \\ u_\theta = (u_{\theta 2} - u_{\theta 1})x + (u_{\theta 3} - u_{\theta 1})y + u_{\theta 1} \end{cases} \begin{cases} \phi = (\phi_2 - \phi_1)x + (\phi_3 - \phi_1)y + \phi_1 \\ \theta = (\theta_2 - \theta_1)x + (\theta_3 - \theta_1)y + \theta_1 \\ u_\phi = (u_{\phi 2} - u_{\phi 1})x + (u_{\phi 3} - u_{\phi 1})y + u_{\phi 1} \\ u_\theta = (u_{\theta 2} - u_{\theta 1})x + (u_{\theta 3} - u_{\theta 1})y + u_{\theta 1} \end{cases} \tag{A6}$$

Where (x, y y) are the corresponding Cartesian coordinate of the point. Conversely, the Cartesian coordinates can be expressed by the Spherical coordinates:

$$\begin{bmatrix} x \\ y \end{bmatrix} = \begin{bmatrix} \theta_3 - \theta_1 & \phi_1 - \phi_3 \\ \theta_1 - \theta_2 & \phi_2 - \phi_1 \end{bmatrix} \begin{bmatrix} \phi - \phi_1 \\ \theta - \theta_1 \end{bmatrix} / Det(A) \quad \begin{bmatrix} x \\ y \end{bmatrix} = \begin{bmatrix} \theta_3 - \theta_1 & \phi_1 - \phi_3 \\ \theta_1 - \theta_2 & \phi_2 - \phi_1 \end{bmatrix} \begin{bmatrix} \phi - \phi_1 \\ \theta - \theta_1 \end{bmatrix} / Det(A)$$
$$A = \begin{bmatrix} \phi_2 - \phi_1 & \phi_3 - \phi_1 \\ \theta_2 - \theta_1 & \theta_3 - \theta_1 \end{bmatrix} \qquad A = \begin{bmatrix} \phi_2 - \phi_1 & \phi_3 - \phi_1 \\ \theta_2 - \theta_1 & \theta_3 - \theta_1 \end{bmatrix} \tag{A7}$$

The derivative of the Cartesian coordinates (x, y) relative to spherical coordinates is constant for linear triangle elements

$$\begin{bmatrix} \partial x/\partial \phi \\ \partial x/\partial \theta \\ \partial y/\partial \phi \\ \partial y/\partial \theta \end{bmatrix} = \begin{bmatrix} \theta_3 - \theta_1 \\ \phi_1 - \phi_3 \\ \theta_1 - \theta_2 \\ \phi_2 - \phi_1 \end{bmatrix} / Det(A) \begin{bmatrix} \partial x/\partial \phi \\ \partial x/\partial \theta \\ \partial y/\partial \phi \\ \partial y/\partial \theta \end{bmatrix} = \begin{bmatrix} \theta_3 - \theta_1 \\ \phi_1 - \phi_3 \\ \theta_1 - \theta_2 \\ \phi_2 - \phi_1 \end{bmatrix} / Det(A) \tag{A8}$$

Thus, the spatial derivative of the velocity in spherical coordinates can be expressed as:

$$\begin{aligned}
\frac{\partial u_\phi}{\partial \phi} &= \frac{\partial u_\phi}{\partial x}\frac{\partial x}{\partial \phi} + \frac{\partial u_\phi}{\partial y}\frac{\partial y}{\partial \phi} = \frac{(u_{\phi 2} - u_{\phi 1})(\theta_3 - \theta_1) + (u_{\phi 3} - u_{\phi 1})(\theta_1 - \theta_2)}{Det(A)} \\
\frac{\partial u_\theta}{\partial \theta} &= \frac{\partial u_\theta}{\partial x}\frac{\partial x}{\partial \theta} + \frac{\partial u_\theta}{\partial y}\frac{\partial y}{\partial \theta} = \frac{(u_{\theta 2} - u_{\theta 1})(\phi_1 - \phi_3) + (u_{\theta 2} - u_{\theta 1})(\phi_2 - \phi_1)}{Det(A)} \\
\frac{\partial u_\phi}{\partial \theta} &= \frac{\partial u_\phi}{\partial x}\frac{\partial x}{\partial \theta} + \frac{\partial u_\phi}{\partial y}\frac{\partial y}{\partial \theta} = \frac{(u_{\phi 2} - u_{\phi 1})(\phi_1 - \phi_3) + (u_{\phi 3} - u_{\phi 1})(\phi_2 - \phi_1)}{Det(A)} \\
\frac{\partial u_\theta}{\partial \phi} &= \frac{\partial u_\theta}{\partial x}\frac{\partial x}{\partial \phi} + \frac{\partial u_\theta}{\partial y}\frac{\partial y}{\partial \phi} = \frac{(u_{\theta 2} - u_{\theta 1})(\theta_3 - \theta_1) + (u_{\theta 2} - u_{\theta 1})(\theta_1 - \theta_2)}{Det(A)} \\
\frac{\partial u_\phi}{\partial \phi} &= \frac{\partial u_\phi}{\partial x}\frac{\partial x}{\partial \phi} + \frac{\partial u_\phi}{\partial y}\frac{\partial y}{\partial \phi} = \frac{(u_{\phi 2} - u_{\phi 1})(\theta_3 - \theta_1) + (u_{\phi 3} - u_{\phi 1})(\theta_1 - \theta_2)}{Det(A)} \\
\frac{\partial u_\theta}{\partial \theta} &= \frac{\partial u_\theta}{\partial x}\frac{\partial x}{\partial \theta} + \frac{\partial u_\theta}{\partial y}\frac{\partial y}{\partial \theta} = \frac{(u_{\theta 2} - u_{\theta 1})(\phi_1 - \phi_3) + (u_{\theta 2} - u_{\theta 1})(\phi_2 - \phi_1)}{Det(A)} \\
\frac{\partial u_\phi}{\partial \theta} &= \frac{\partial u_\phi}{\partial x}\frac{\partial x}{\partial \theta} + \frac{\partial u_\phi}{\partial y}\frac{\partial y}{\partial \theta} = \frac{(u_{\phi 2} - u_{\phi 1})(\phi_1 - \phi_3) + (u_{\phi 3} - u_{\phi 1})(\phi_2 - \phi_1)}{Det(A)} \\
\frac{\partial u_\theta}{\partial \phi} &= \frac{\partial u_\theta}{\partial x}\frac{\partial x}{\partial \phi} + \frac{\partial u_\theta}{\partial y}\frac{\partial y}{\partial \phi} = \frac{(u_{\theta 2} - u_{\theta 1})(\theta_3 - \theta_1) + (u_{\theta 2} - u_{\theta 1})(\theta_1 - \theta_2)}{Det(A)}
\end{aligned} \tag{A9}$$

With the spatial derivatives of the velocities under spherical coordinates, the strain rates under the spherical coordinates can be calculated (A1-A5).

Appendix B. Cumulative Deformation

After the deforming network is constructed and the strain rate is computed, the evolution of a set of quantities (finite strain, crustal thickness, lithospheric temperature, isostatic topography and heat flux)

can be calculated for a set of user-specified points (strain markers). Comparison of these quantities against observations allows the user to update the deforming network interactively. The mathematical details on each of the integrated quantities is given below. At present, *GPlates* 2.1 only outputs crustal thickness (stretching factor, thinning factor) and finite strain, but other quantities have been used previously to update the deforming network in southeast Asia (Yang et al., 2016).

Assuming that a lithospheric block is incompressible in 3D space, that is, there is no net mass generation or loss during its deformation with horizontal divergence or convergence generating vertical thinning or thickening, then the crustal thickness H evolution of the lithospheric block meets the mass conservation equation:

$$\frac{DH}{Dt} = -H \cdot \dot{S} \; \frac{DH}{Dt} = -H \cdot \dot{S} \tag{B1}$$

Here $\dot{S} = \nabla \cdot \vec{u} = \dot{\varepsilon}_D \; \dot{S} = \nabla \cdot \vec{u} = \dot{\varepsilon}_D$ is the surface dilatation rate of this crustal block. With the dilatation rate at each time from deforming network reconstruction, the above ordinary differential equation is solved with the Runge-Kutta Method in *GPlates*. The dilatation rate is calculated under the spherical coordinate in *GPlates*, although calculating it under the Cartesian coordinate gives little difference in crustal thickness evolution. The Beta (or stretching factor), $\beta = \exp(\int_0^t \dot{S}(t)\,dt) \; \beta = \exp(\int_0^t \dot{S}(t)\,dt)$ is also computed.

In many geological problems, the displacement gradient (strain) is comparable to unity although the strain rate is far less than unity. In these cases, the infinitesimal strain assumption is not suitable anymore and finite strain is calculated. The strain tensor is defined in the finite strain regime as (Malvern, 1969):

$$\varepsilon = \frac{1}{2}[\mathbf{F}^T\mathbf{F} - \mathbf{I}] \tag{B5}$$

Where

$$\mathbf{F} = \mathbf{x}\bar{\nabla} = \mathbf{I} + \mathbf{u}\bar{\nabla} \; \mathbf{F} = \mathbf{x}\bar{\nabla} = \mathbf{I} + \mathbf{u}\bar{\nabla} \tag{B6}$$

is the deformation gradient tensor. **x** and **u** are position and displacement vectors, respectively. The rate of the deformation gradient tensor change is

$$\dot{\mathbf{F}} = \mathbf{LF}\ \dot{\mathbf{F}} = \mathbf{LF} \tag{B7}$$

Where $\mathbf{L} = \mathbf{v}\bar{\nabla}_{\mathbf{x}}\ \mathbf{L} = \mathbf{v}\bar{\nabla}_{\mathbf{x}}$ is the spatial gradients of velocity. Given the velocity field, and the initial deformation gradient tensor (identity matrix if un-deformed), we can calculate F with the Runge-Kutta method. The two principal strains are (Malvern, 1969)

$$\begin{aligned}\lambda_{1,2} &= 0.5\{F_{1,1}^2 + F_{1,2}^2 + F_{2,1}^2 + F_{2,2}^2 \pm \sqrt{(F_{1,1}^2 + F_{1,2}^2 + F_{2,1}^2 + F_{2,2}^2)^2 - 4(F_{1,1}F_{2,2} - F_{1,2}F_{2,1})^2}\} \\ \lambda_{1,2} &= 0.5\{F_{1,1}^2 + F_{1,2}^2 + F_{2,1}^2 + F_{2,2}^2 \pm \sqrt{(F_{1,1}^2 + F_{1,2}^2 + F_{2,1}^2 + F_{2,2}^2)^2 - 4(F_{1,1}F_{2,2} - F_{1,2}F_{2,1})^2}\}\end{aligned} \tag{B8}$$

The angle of the principal strain axis from longitude direction after deformation is determined by

$$\tan 2\theta = 2(F_{1,1}F_{2,1} + F_{1,2}F_{2,2})/(F_{1,1}^2 + F_{1,2}^2 - F_{2,1}^2 - F_{2,2}^2) \tag{B9}$$

Figure Captions

Figure. 1. A. Geological data and concepts used in the reconstruction. B. Their computer representation. C. The continuously closed plate in the computer representation. In A we have a deformation region (D_1) that is part of plate 1 (P_1). D_1 is bound by a subducting margin on its left hand side and an extending region on its right hand side. The normal faults denote the diffuse boundary between D_1 and P_1. The top and bottom boundaries mostly accommodate transform motion. Within D_1 there is a collection of deformation points (filled circles), normal faults, and rigid blocks (RB). Points and lines within the interior are shown in orange while those on the boundary are in black. The displacements u_3, u_4, u_n… are with respect to fixed plate P_1. In B we show the computer implementation of the deforming region that is consistent with the concepts of a continuously closing plate (CCP, Gurnis et al., 2012). First, the outer boundary of D_1 is a topological closed polygon with the intersection points found at each moment of time. The triangular Delaunay mesh shown in green then represents the continuous deformation within D_1. Linear interpolation is used to find the velocity and displacements within the mesh. In C the CCP is shown as the blue polygon.

Figure 2. Flowchart of the time integration of deformation in *GPlates* 2.1. Step 1 is the backward integration of the position of strain markers to obtain their initial position in the deformation topological network. Step 2 is the forward integration of the finite strain tensor to obtain the deformation history of the strain marker.

Figure 3. Reconstruction of western North America from 36 Ma to the present using *GPlates 2.1* deforming networks with global plate motions, with rigid North America held fixed. The original digital reconstruction was imported from McQuarrie and Wernicke (2005) and then modified to the north and south as described in the text. A. Displacement points and displacement vectors at 0 Ma.

Triangular mesh with dilatational strain rate at 0 Ma (B) and at 35 Ma (C.) D. Predicted finite strain markers resulting from the integration through the deforming network from 36 Ma to the present overlaying the smoothed dilatation strain rate. Outlines of rigid blocks filled with solid blue. Pacific (PAC), stable North America (NAM), Farallon (FAR), Vancouver (VAN), and Juan de Fuca (JdF) plates are labeled, along with Basin and Range province (BR), the Sierra Nevada block (SN), the Colorado Plateau (CP), the Cascadia volcanic arc (Cas), and the Klamath Mountains (Kla). Spacing between latitude and longitude graticules is 15°. Each sub-panel produced with *GPlates* 2.1.

Figure 4. Global perspective of the North America deforming topological network at 26 Ma. Pacific (PAC), stable North America (NAM), Farallon (FAR) and Juan de Fuca (JdF) plates are labeled. Rigid plates in a moving hot-spot frame of reference (e.g. Müller et al., 2016a) shown. Velocity of different plates have different colors. Note that some of the plate velocity within the deforming network also shown. Spacing between latitude and longitude graticules is 30°. Produced with *GPlates* 2.1.

Figure 5. Reconstruction of southeast Asia from Yang *et al*. (2016) with respect to stable China. A. Deformation network in grey with basin outlines in black overlaying present day topography. Tectonic subsidence curves from eight basins (position shown with small red dots) are used to construct the southeast Asia deforming network (see Yang et al. (2016) for details). Dilatational strain rate shown with basin boundaries in black at present (B) and at 30 Ma (C). Finite strain markers overlain in B. Forward prediction of beta factor (D) and finite strain variations (B) by integrating strain markers through the deformation network form 40 Ma to the present. Labeled are: Borneo (Bo), Malay peninsula (Ma), Sunda Shelf (SS) and the stable China (SC), Australian (AUS) and West

Philippine (WPP) plates. Spacing between latitude and longitude graticules is 30°. All subpanel images produced with *GPlates* 2.1.

Figure 6. Deformation model of South Atlantic passive margin and predictions. Zoom into the central South Atlantic showing the tessellation and displacement vectors in the South America frame of reference at 125 Ma (A) and 120 Ma (B). Same region but in the mantle fixed frame of reference showing the dilatational strain rate (C) and total topography from Flament et al. (2014) (D). The topography was computed external to *GPlates*. The SAM plate is the fixed frame of reference. The South American (SAM) and African (AFR) plates are labeled; in C deforming crust is denoted with DC and stable passive margins with P. Spacing between latitude and longitude graticules is 30°. All subpanel images produced with *GPlates* 2.1.

References

Arriagada, C., Roperch, P., Mpodozis, C., Cobbold, P. R., 2008. Paleogene building of the Bolivian Orocline: Tectonic restoration of the central Andes in 2-D map view. Tectonics 27, TC6014, doi:10.1029/2008TC002269.

Atwater, T., Stock, J., 1998. Pacific–North America Plate tectonics of the Neogene southwestern United States; an update, In Ernst, W.G., and Nelson, C.A. (Ed) Integrated Earth and environmental evolution of the southwestern United States: The Clarence A. Hall, Jr. volume, Columbia, Bellwether Publishing, pp. 393–420.

Boyden, J. A., Müller, R. D., Gurnis, M., Torsvik, T. H., Clark, J. A., Turner, M., Ivey-Law, H., Watson, R. J., Cannon, J. S., 2011. Next-generation plate-tectonic reconstructions using GPlates, In Keller, G. R., Baru, C. (Ed) Geoinformatics: Cyberinfrastructure for the Solid Earth Sciences, Cambridge University Press, pp. 95-113.

Bower, D. J., Gurnis, M., Flament, N., 2015. Assimilating lithosphere and slab history in 4-D dynamic Earth models. Physics of Earth and Planetary Interiors 238, doi: 10.1016/j.pepi.2014.10.013, 8–22.

Bunge, H.-P., Richards , M. A., Baumgardner, J. R., 2002. Mantle-circulation models with sequential data assimilation: inferring present-day mantle structure from plate-motion histories. Philosophical Transactions of the Royal Society of London, A 360, 2545–2567.

Cottam, M.A., Hall, R., Ghani, A.A., 2013. Late Cretaceous and Cenozoic tectonics of the Malay Peninsula constrained by thermochronology. Journal of Asian Earth Sciences 76, 241-257.

Doust, H., Sumner, H.S., 2007. Petroleum systems in rift basins–a collective approach in Southeast Asian basins. Petroleum Geoscience 13(2), 127-144.

Dunbar, J. A., Sawyer, D. S., 1987. Implications of continental crust extension for plate reconstruction: An example from the Gulf of Mexico, Tectonics 6, 739-755.

Fabri, A., Pion, S., 2009. CGAL: the Computational Geometry Algorithms Library, Proceedings of the 17th ACM SIGSPATIAL International Conference on Advances in Geographic Information Systems. ACM, Seattle, Washington, pp. 538-539, doi: 10.1145/1653771.1653865

Flament, N., Gurnis, M., Williams, S., Seton, M., Skogseid, J., Heine, C., Müller, R. D., 2014. Topographic asymmetry of the South Atlantic from global models of mantle flow and lithospheric stretching. Earth and Planetary Science Letters 387, 107–119, doi: 10.1016/j.epsl.2013.11.017.

Fuller, M., Ali, J., Moss, S., Frost, G., Richter, B., Mahfi, A., 1999. Paleomagnetism of Borneo. Journal of Asian Earth Science 17, 3–24, doi:10.1016/S0743-9547(98)00057-9.

Goddéris, Yves, et al., 2014. The role of palaeogeography in the Phanerozoic history of atmospheric CO2 and climate. Earth-Science Reviews, 128, 122-138.

Gordon, R. G., Stein, S., 1992. Global tectonics and space geodesy. Science 256, 333-340.

Gurnis, M., Turner, M., Zahirovic, S., DiCaprio, L., Spasojevic, S., Müller, R. D., Boyden, J., Seton, M., Manea, V. C., and Bower, D. J., 2012. Plate tectonic reconstructions with continuously closing plates. Computers & Geosciences 38, 35-42, doi: 10.1016/j.cageo.2011.04.014.

Hall, R., 2002. Cenozoic geological and plate tectonic evolution of SE Asia and the SW Pacific: computer-based reconstructions, model and animations. Journal of Asian Earth Sciences 20(4), 353-431.

Hall, R., Morley, C. K., 2004. Sundaland basins, in Continent-Ocean Interactions within East Asian Marginal Seas, In Clift, P., et al. (Ed). Geophysical Monograph Series, American Geophysical Union, Washington, D. C., pp. 55–85.

Heine, C., Zoethout, J., Müller,R. D., 2013. Kinematics of the South Atlantic rift, Solid Earth Discussion 4, 215–253, doi: 10.5194/se-4-215-2013.

Hughes, T. J. R., 2000. The Finite Element Method: Linear Static and Dynamic Finite Element Analysis, Dover Publications, Mineola, New York, 682 pp.

Kneller, E., Johnson, C. A., Karner, G. D., Einhorn, J., Queffelec, T. A., 2012. Inverse methods for modeling non-rigid plate kinematics: Application to Mesozoic plate reconstructions of the Central Atlantic, Computers & Geosciences 49, 217-230, doi: 10.1016/j.cageo.2012.06.019.

Kreemer, C., Holt, W. E., Haines, A. J., 2003. An integrated global model of present-day plate motions and plate boundary deformation. Geophysical Journal International 154, 8–34.

Kreemer, C., Blewitt, G., Klein, E. C., 2014. A geodetic plate motion and Global Strain Rate Model. Geochemistry Geophysics Geosystems 15, 3849–3889, doi: 10.1002/2014GC005407.

Lawver, L. A., 2001. The PLATES 2001 Atlas of Plate Reconstructions: 750 Ma to Present Day, UTIG Technical Report, University of Texas, Austin, Texas.

Lee, T. Y., Lawver, L. A., 1994. Cenozoic plate reconstruction of the South China Sea region. Tectonophysics 235, 149-180.

Lunt, D. J., Huber, M., Anagnostou, E., Baatsen, M. L. J., Caballero, R., DeConto, R., Dijkstra, H. A., et al., 2017. The DeepMIP contribution to PMIP4: experimental design for model simulations of the EECO, PETM, and pre-PETM (version 1.0), Geoscientific Model Development 10, 889-901, doi: 10.5194/gmd-10-889-2017.

Malvern, L. E., 1969. Introduction to the Mechanics of a Continuous Media. Prentice-Hall, Inc., Upper Saddle River, NJ. 713 pp.

McQuarrie, N., Wernicke, B. P., 2005. An animated tectonic reconstruction of southwestern North America since 36 Ma. Geosphere 1, 147-172, doi: 10.1130/GES00016.1.

Metcalfe, I., 2011. Tectonic framework and Phanerozoic evolution of Sundaland. Gondwana Research 19(1), 3-21.

Morley, C. K., 2002, A tectonic model for the Tertiary evolution of strike–slip faults and rift basins in SE Asia. Tectonophysics 347, 189-215

Moucha, R., Forte, A. M., Rowley, D. B., Mitrovica, J. X., Simmons, N. A., and Grand, S. P., 2008.Mantle convection and the recent evolution of the Colorado Plateau and the Rio Grande Rift valley. Geology 36, 439–442; doi: 10.1130/G24577A.1.

Müller, R. D., Seton, M., Zahirovic,S., Williams, S. E., Matthews, K. J., Wright, N. M., Shephard, G. E., Maloney, K. T., Barnett-Moore, N., Hosseinpour, M., Bower, D. J., and Cannon, J., 2016a, Ocean basin Eevolution and global-scale plate reorganization events since Pangea breakup, Annual Review of Earth and Planetary Science 44, 107–138, 10.1146/annurev-earth-060115-012211.

Müller, R.D., Qin, X., Sandwell, D.T., Dutkiewicz, A., Williams, S.E., Flament, N., Maus, S. and Seton, M., 2016b. The GPlates Portal: Cloud-based interactive 3D visualization of global geophysical and geological data in a web browser, PLoS ONE 11(3), e0150883. doi:10.1371/ journal.pone.0150883

Péron-Pinvidic, G., Manatschal, G., 2009. The final rifting evolution at deep magma-poor passive margins from Iberia-Newfoundland: a new point of view. International Journal of Earth Sciences 98, 1581-1597.

Replumaz, A., Tapponnier, P., 2003. Reconstruction of the deformed collision zone between India and Asia by backward motion of lithospheric blocks. Journal of Geophysical Research108, doi:10.1029/2001JB000661.

Seton, M., Müller, R.D., Zahirovic, S., Gaina, C., Torsvik, T., Shephard, G., Talsma, A., Gurnis, M., Turner, M., Maus, S., Chandler, M., 2012. Global continental and ocean basin reconstructions since 200Ma. Earth-Science Reviews 113(3), 212-270.

Simons, W.J.F., Socquet, A., Vigny, C., Ambrosius, B.A.C., Haji Abu, S., Promthong, C., Subarya, C., Sarsito, D.A., Matheussen, S., Morgan, P., Spakman, W., 2007. A decade of GPS in Southeast Asia: Resolving Sundaland motion and boundaries. Journal of Geophysical Research: Solid Earth 112, doi: 10.1029/2005JB003868.

Srivastava, S. P., Verhoef, J, 1992. Evolution of Mesozoic sedimentary basins around the North Central Atlantic: a preliminary plate kinematic solution. Geological Society, London, Special Publications 62 (1), 397-420.

Thatcher, W., How the continents deform: The evidence from tectonic geodesy. Annual Review of Earth and Planetary Science 37, 237-262, doi: 10.1146/annurev.earth.031208.100035, 2009.

The CGAL Project, 2017, User and Reference Manual, **CGAL Editorial Board**, 4.10.1 ed., http://doc.cgal.org/4.10.1/Manual/packages.html.

Torsvik, T.H., Smethurst, M. A., Plate tectonic Modelling: virtual reality with GMAP, Computers & Geosciences, 25, 395-402, 1999

Unternehr, P., Curie, D., Olivet, J. L., Goslin, J., Beuzart, P., 1988. South Atlantic fits and intraplate boundaries in Africa and outh America, Tectonophyics 155, 169-179.

Wernicke, B., Snow, J.K., 1998. Cenozoic tectonism in the central Basin and Range: Motion of the Sierran–Great Valley Block. International Geology Review 40, 403–410.

Wernicke, B., Axen, G.J., Snow, J.K., 1988. Basin and Range extensional tectonics at the latitude of Las Vegas, Nevada. Geological Society of America Bulletin,100, 1738–1757, doi: 10.1130/0016-7606(1988)100**,**1738:BARETA**.**2.3.CO;2.

Wessel, P., Müller, R.D., 2015. Plate tectonics. In: G. Schubert (Ed) Treatise on Geophysics, Second edition*, 6, Elsevier,* 45-93.

Williams, S., Müller, R.D., Landgrebe, T. C.W., Whittaker, J.M., 2012. An open-source software environment for visualizing and refining plate tectonic reconstructions using high resolution geological and geophysical data sets. GSA Today 22 (4/5), 4-9, doi: 10.1130/GSATG139A.1

Williams, S. E., J. M. Whittaker, and R. D. Müller, Full-fit, palinspastic reconstruction of the conjugate Australian-Antarctic margins. Tectonics 30, TC6012, doi:10.1029/2011TC002912, 2011.

Xu, J., Ben-Avraham, Z., Kelty, T., Yu, H.-S., 2014. Origin of marginal basins of the NW Pacific and their plate tectonic reconstructions. Earth-Science Reviews, 130, 154–196, doi: 10.1016/j.earscirev.2013.10.002.

Yang, T., Gurnis, M., Zahirovic, S., 2016. Mantle induced subsidence and compression in SE Asia since the early Miocene. Geophysical Research Letters 43, 1-9, doi:10.1002/2016GL068050.

Zahirovic, S., Seton, M., and Müller, R. D., 2014. The Cretaceous and Cenozoic tectonic evolution of Southeast Asia. Solid Earth 5, 227–273, doi:10.5194/se-5-227-2014.

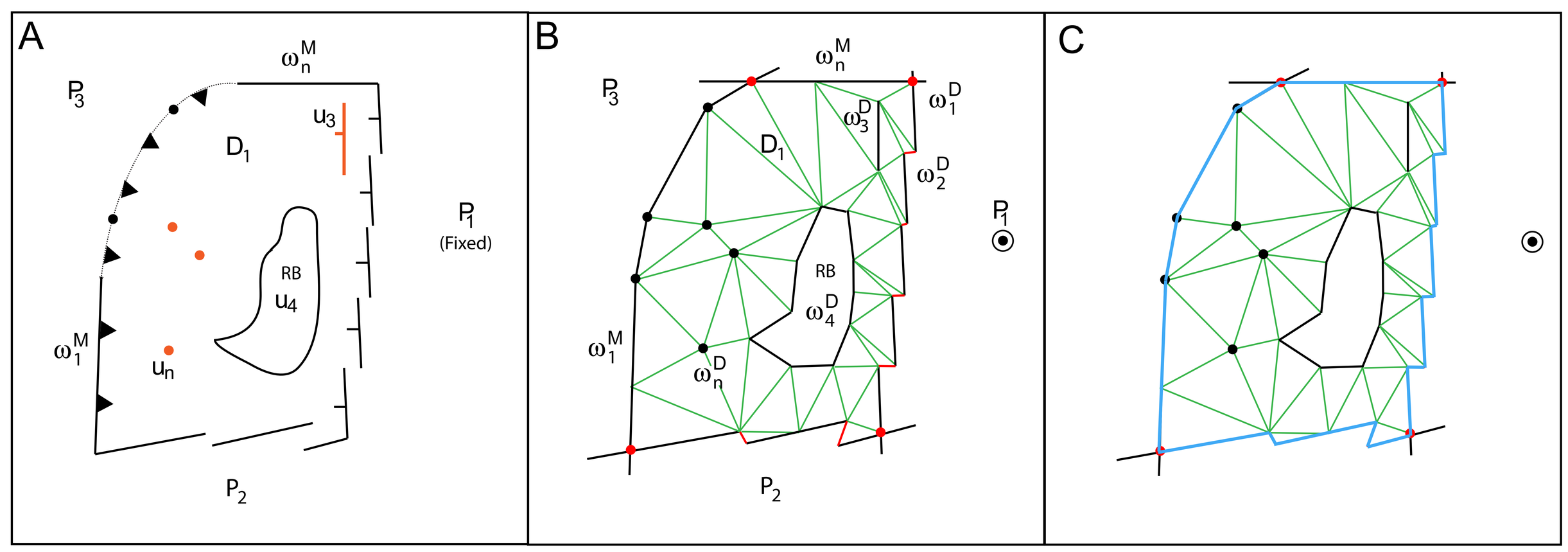
A
ω_n^M
P_3
u_3
D_1
P_1
(Fixed)
RB
u_4
ω_1^M
u_n
P_2
B
ω_n^M
P_3
ω_1^D
ω_3^D
D_1
ω_2^D
P_1
RB
ω_4^D
ω_1^M
ω_n^D
P_2
C

Reconstruction and deformation within topological networks (deforming plates)

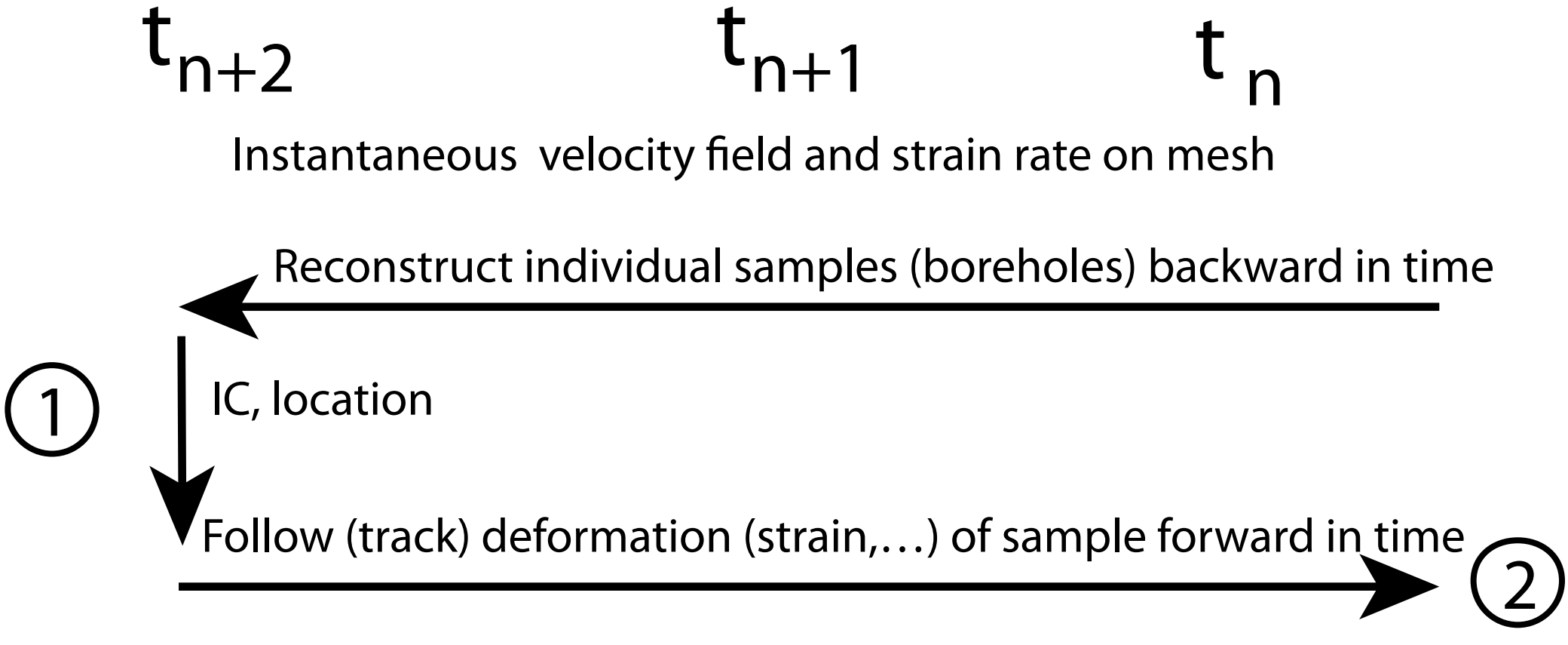

A

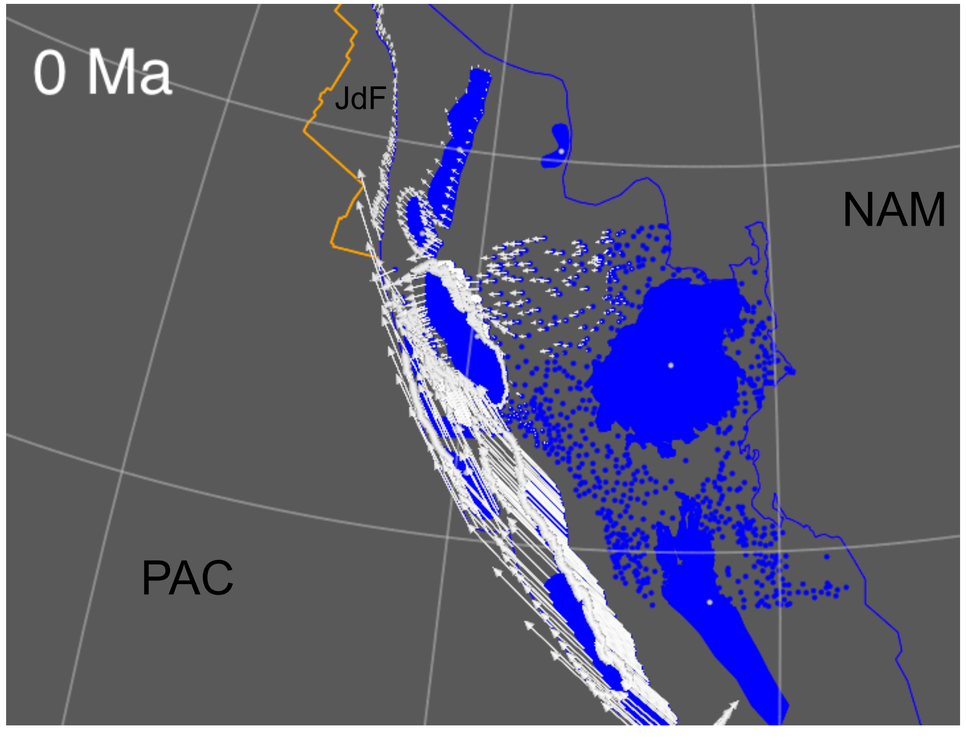

B

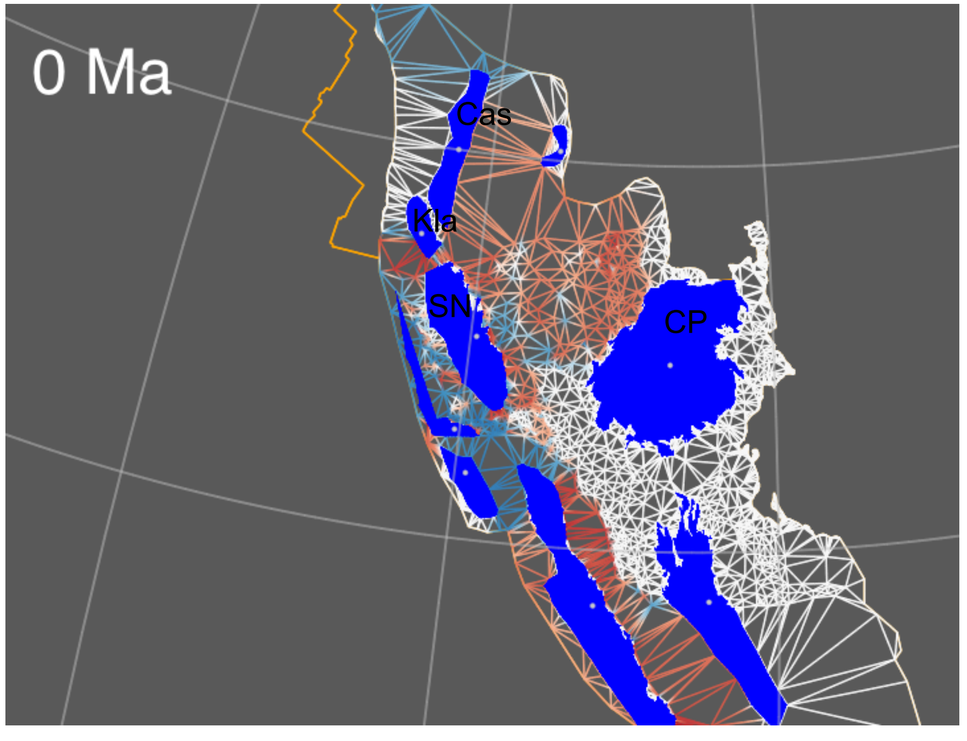

Strain rate (s^{-1})

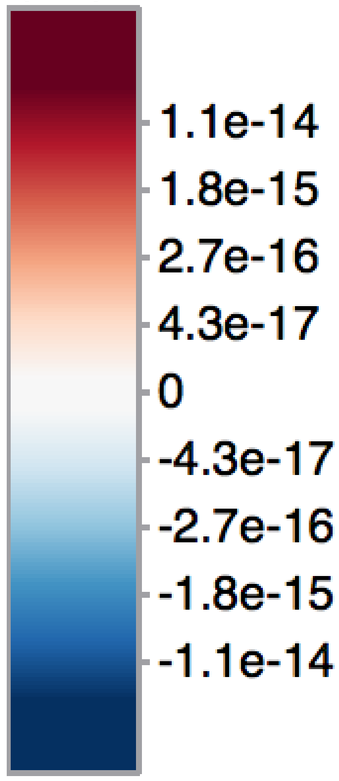

C

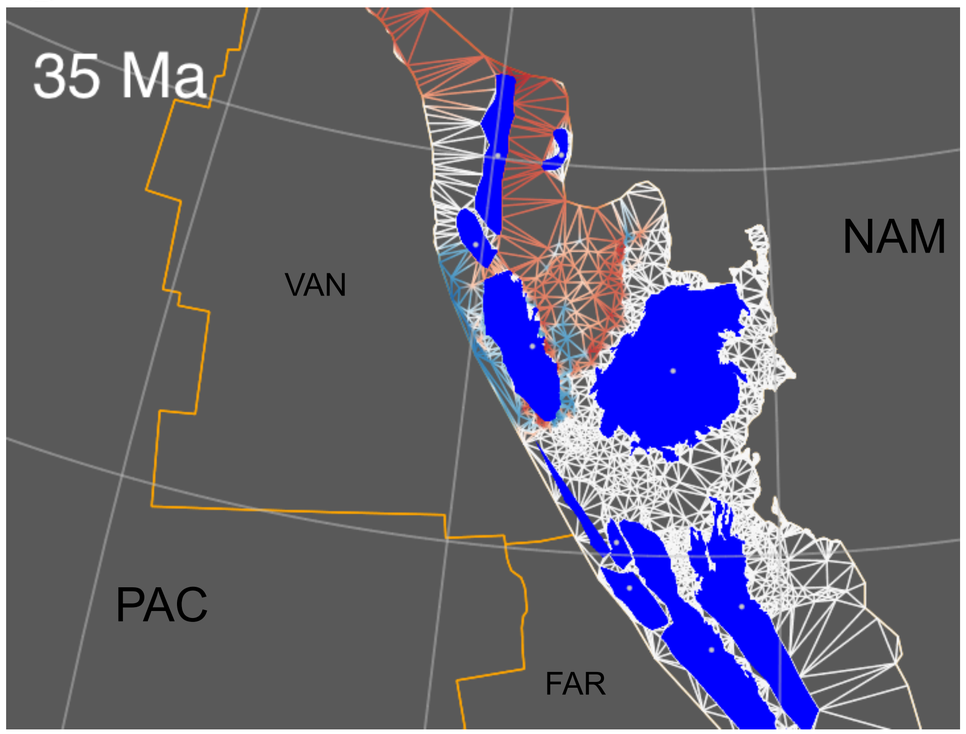

D

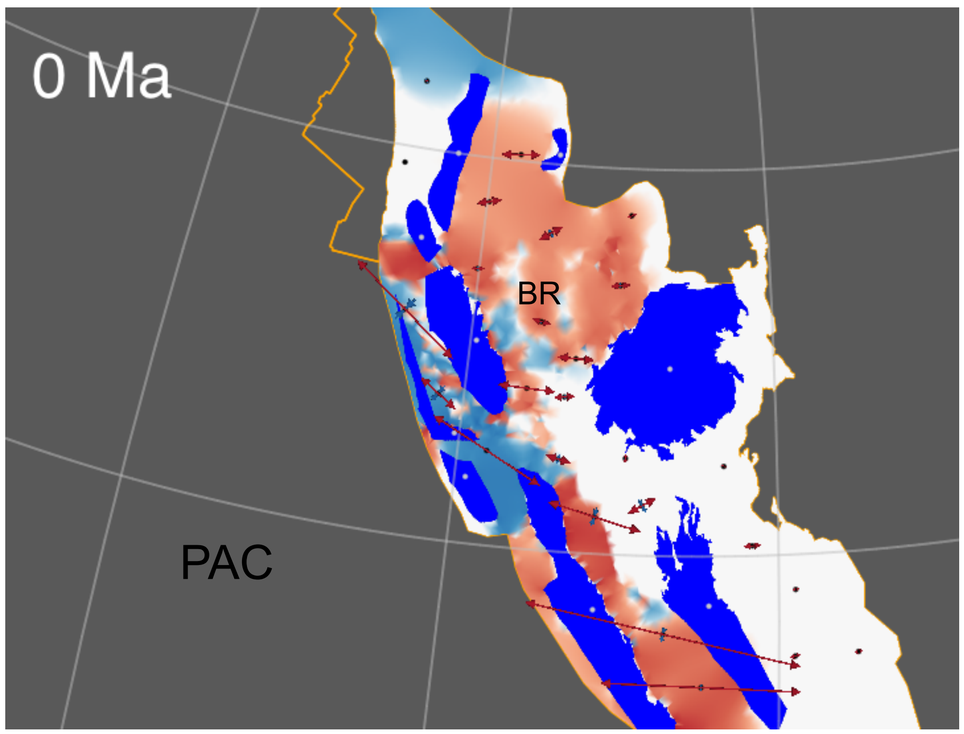

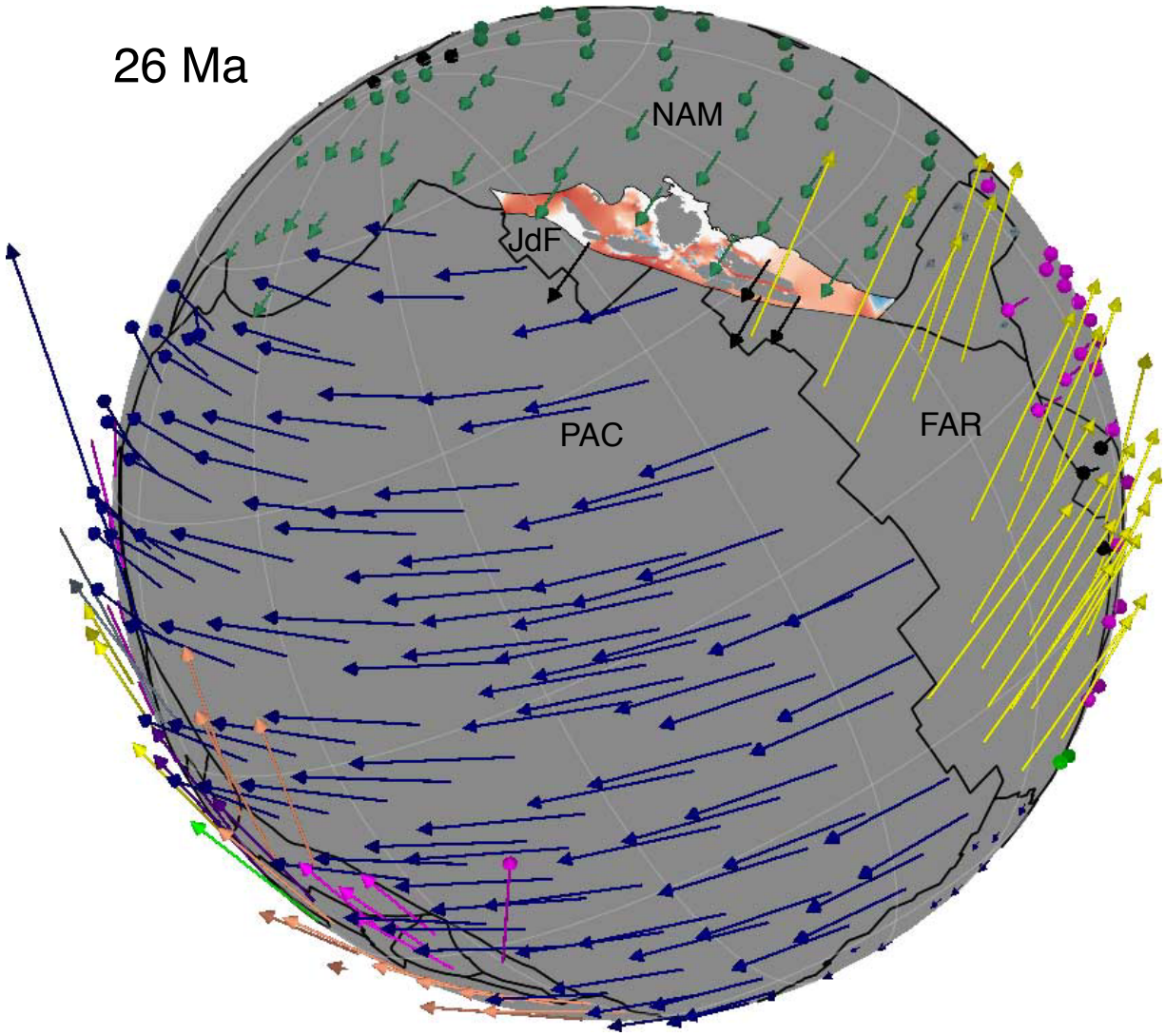
26 Ma
NAM
JdF
PAC
FAR

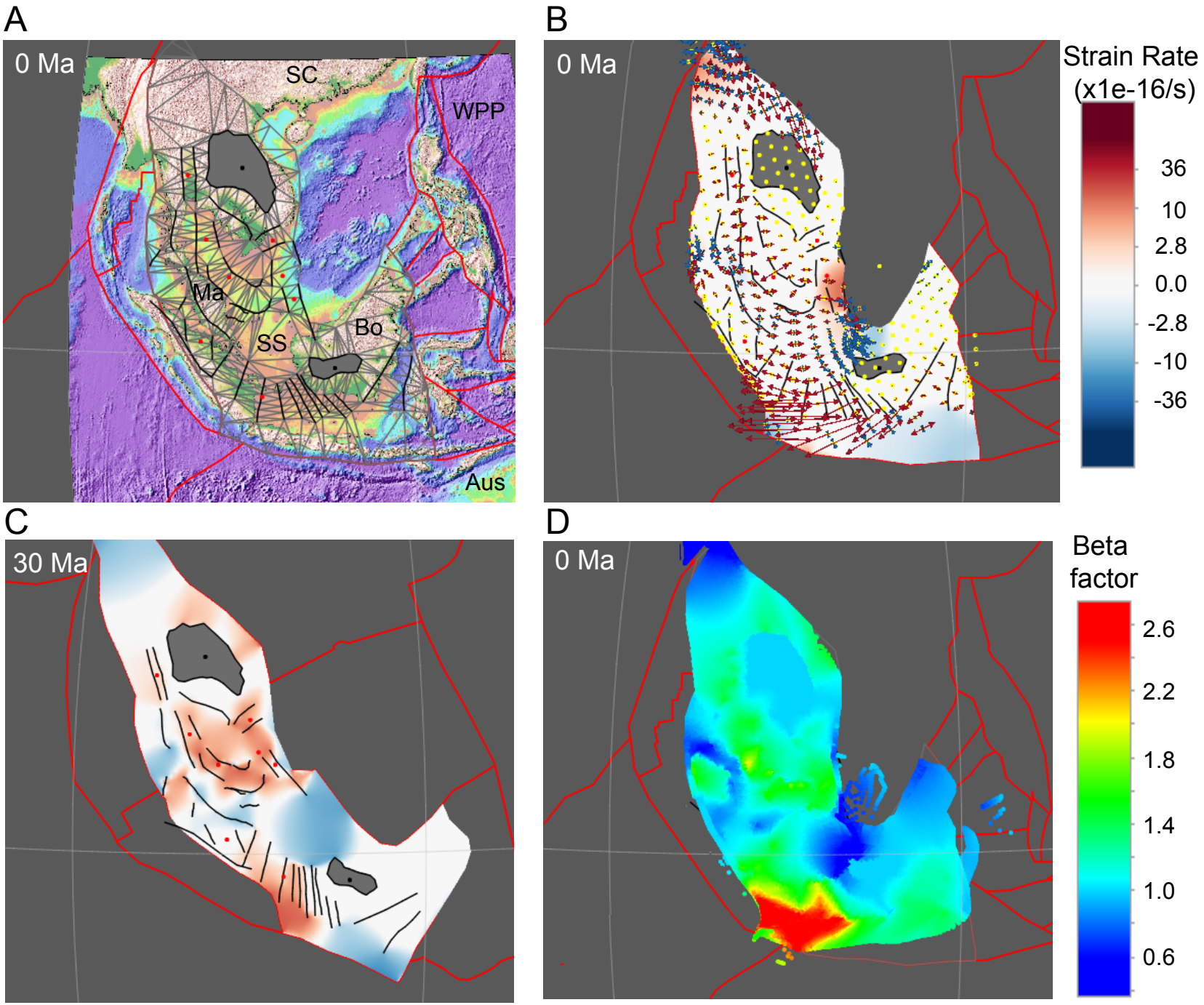
A
0 Ma
SC
WPP
Ma
SS
Bo
Aus
B
0 Ma
Strain Rate
(x1e-16/s)
36
10
2.8
0.0
-2.8
-10
-36
C
30 Ma
D
0 Ma
Beta
factor
2.6
2.2
1.8
1.4
1.0
0.6

A

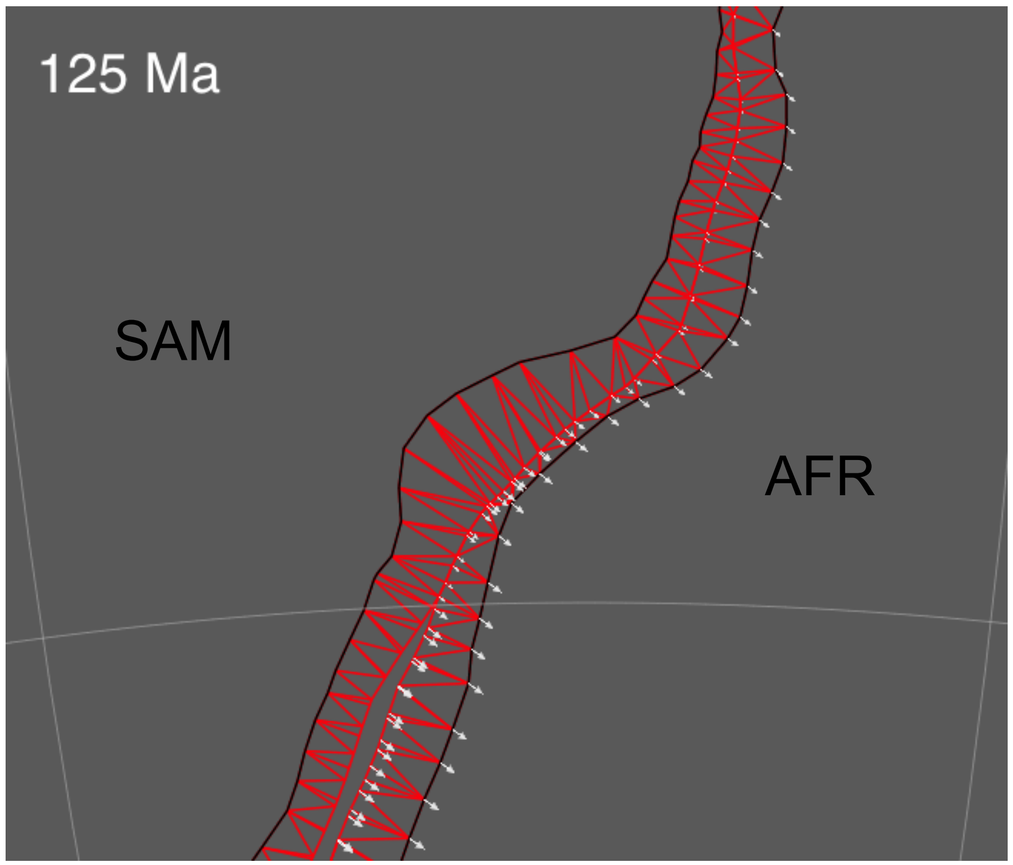
125 Ma
SAM
AFR

B

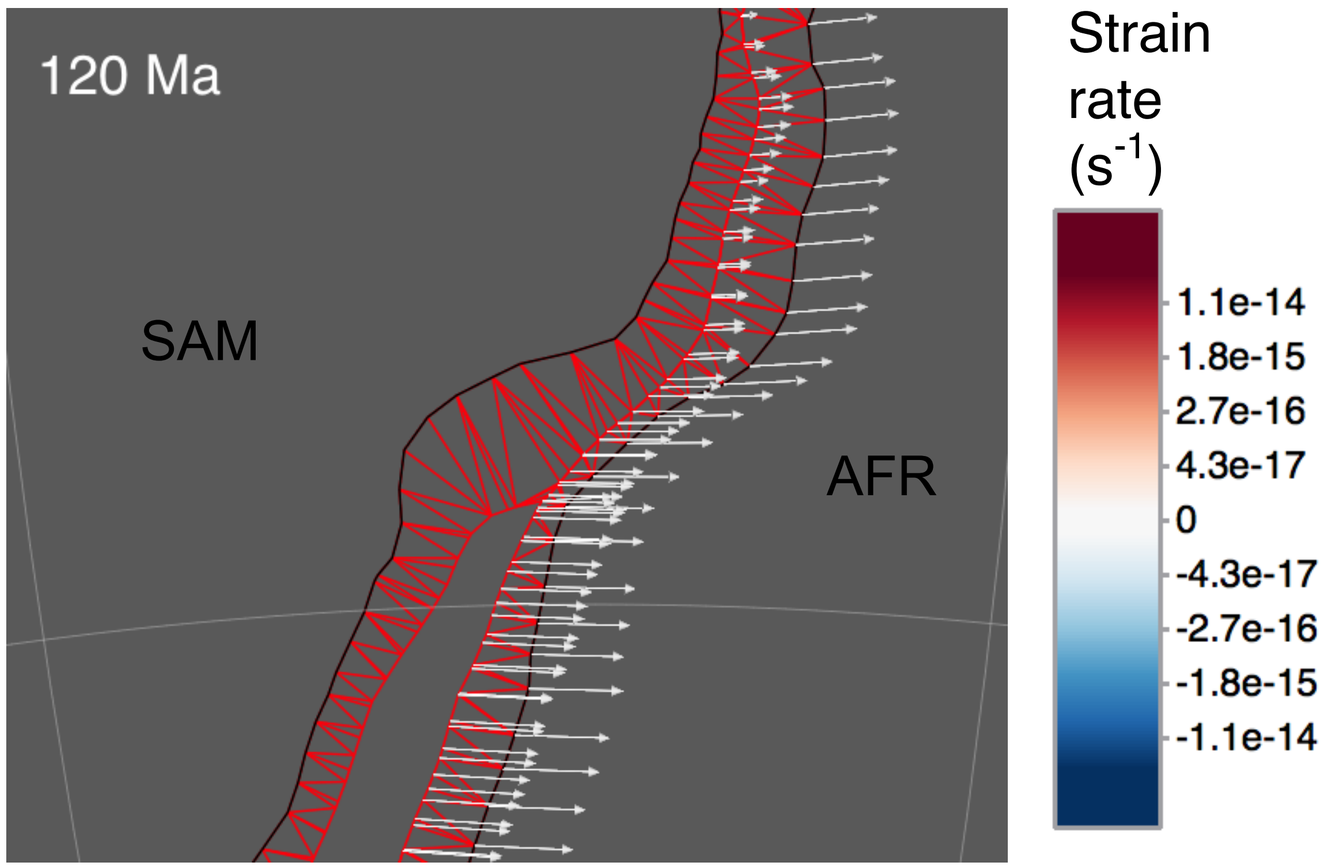
120 Ma
SAM
AFR
Strain rate (s^{-1})
1.1e-14
1.8e-15
2.7e-16
4.3e-17
0
-4.3e-17
-2.7e-16
-1.8e-15
-1.1e-14

C

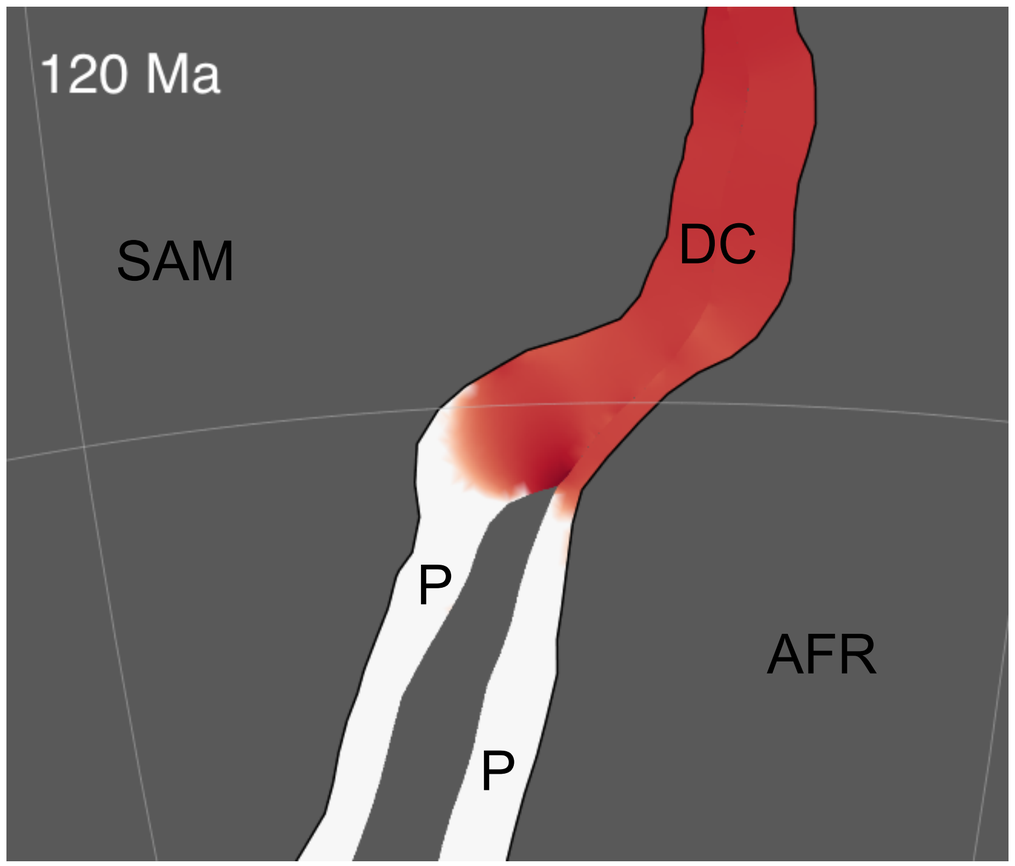
120 Ma
SAM
DC
P
P
AFR

D

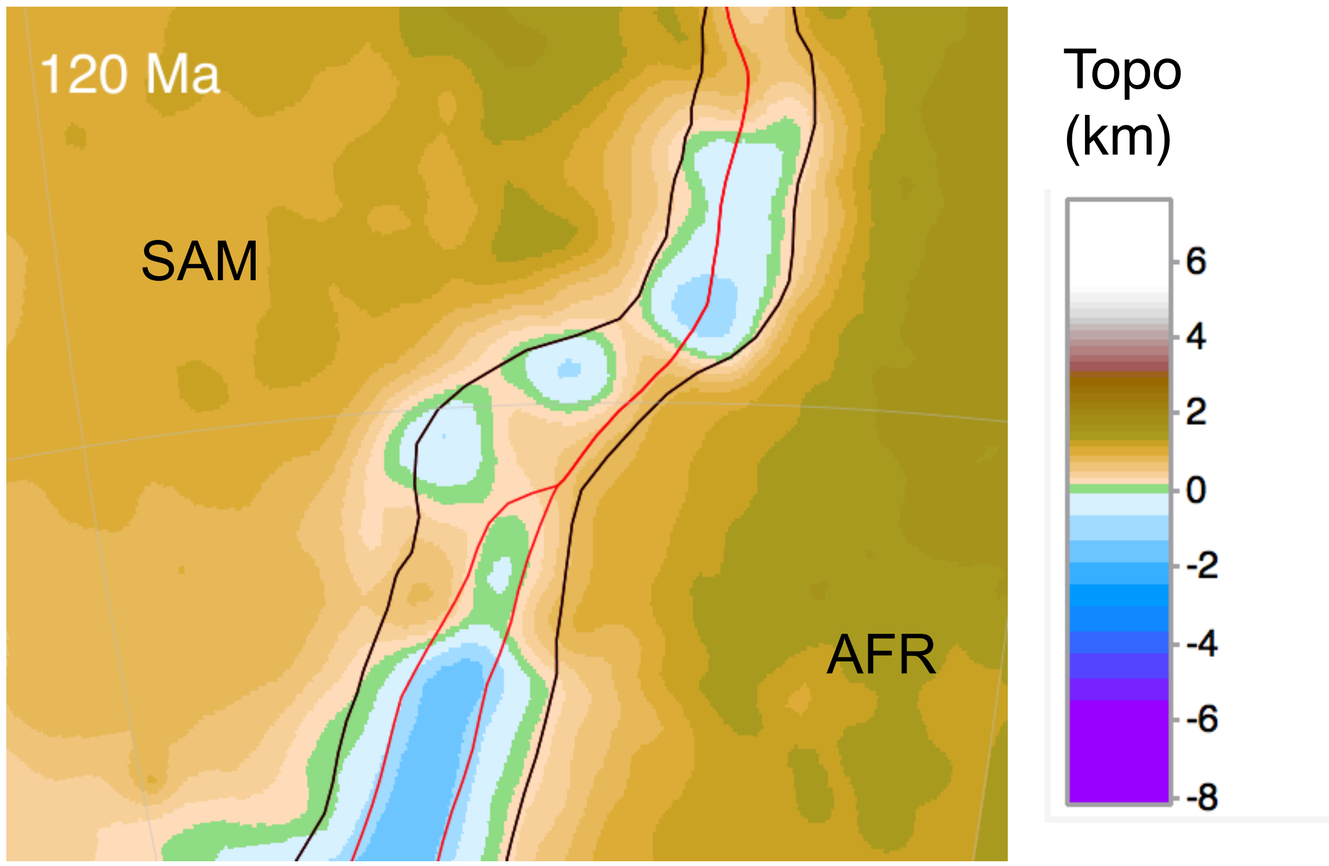
120 Ma
SAM
AFR
Topo (km)
6
4
2
0
-2
-4
-6
-8